Volume 17
Number 12
25 March 2026
Pages 5763–6244

Chemical Science

rsc.li/chemical-science

ISSN 2041-6539

ROYAL SOCIETY OF CHEMISTRY

EDGE ARTICLE

Ao Xia *et al.*

Engineering a semi-artificial photosynthetic biofilm for robust and high-efficiency CO_2-to-methane conversion

Chemical Science

ROYAL SOCIETY OF CHEMISTRY

EDGE ARTICLE

View Article Online
View Journal | View Issue

Cite this: *Chem. Sci.*, 2026, **17**, 5857

All publication charges for this article have been paid for by the Royal Society of Chemistry

Engineering a semi-artificial photosynthetic biofilm for robust and high-efficiency CO_2-to-methane conversion

Huize Chen,[ab] Ao Xia,[*ab] Yun Huang,[ab] Junyi Ji,[c] Jingmiao Zhang,[ab] Xianqing Zhu,[ab] Xun Zhu[ab] and Qiang Liao[ab]

Received 16th January 2026
Accepted 19th February 2026

DOI: 10.1039/d6sc00459h

rsc.li/chemical-science

Hybrid semi-artificial photosynthetic systems, which integrate semiconductor nanomaterials with methanogens, offer an innovative strategy for the solar-driven conversion of CO_2 to CH_4 with high selectivity. However, these systems face challenges, including light harvesting losses, low quantum efficiency, and instability due to photodamage. To overcome the intrinsic limitations, we introduce a paradigm-shifting strategy: leveraging biofilms as a new platform for efficient solar-driven CO_2-to-CH_4 conversion. The strategic modification of carbon nitride promoted the self-assembly of stable biofilms. This process formed an integrated, cross-linked network comprising the material, cells, and extracellular polymeric substances, which remarkably improved light utilization efficiency compared to traditional suspension systems. Furthermore, the extracellular polymeric substance matrix served as a biocompatible shield, effectively quenching reactive oxygen species and suppressing photodamage to the cells. To further enhance efficiency, *Methanosarcina barkeri* was decorated with silver nanoparticles. This modification rewires the electron transfer pathway, promoting a ferredoxin-independent mechanism and significantly enhancing cellular electron uptake. We achieved a state-of-the-art performance with a record 1.92% quantum yield and 97.1% methane selectivity by suppressing photodamage. This study pioneers the paradigm of integrating biofilms within hybrid systems. By elucidating its advantages and potential applications, our work provides a foundational blueprint for engineering the hybrid-biofilm microenvironment and designing practically viable reactors.

Introduction

The urgent need to mitigate atmospheric CO_2 levels and transition towards sustainable chemical production has spurred intense research into novel carbon-neutral technologies. Semi-artificial photosynthetic systems are novel platforms that couple microorganisms with light-absorbing synthetic materials, leveraging the photophysics of the synthetic materials and the selectivity and metabolic precision of microbial systems to realize highly selective and sustainable solar-to-chemical energy conversion under mild conditions.[1,2] This system demonstrates significant potential for energy production,[3,4] pollutant degradation,[5,6] and high-value chemical production.[7,8] Recent studies have demonstrated that methanogens can utilize photogenerated electrons from semiconductors through direct contact to enable highly selective CO_2-to-CH_4 conversion.[3,9,10]

However, existing suspended hybrid systems are inherently limited by two critical challenges: light transfer limitations and photodamage. In such systems, the loose coupling between semiconductor materials and cells leads to significant light scattering, ineffective absorption, and shielding.[3,11–14] Intrinsic light absorption by the aqueous medium further exacerbates photon loss, collectively reducing the system's overall light utilization efficiency. Conversely, strategies aimed at enhancing performance by increasing incident light intensity inevitably cause microbial photodamage, thereby severely compromising long-term operational stability.[15,16] Such damage stems from direct radiation-induced damage to cellular components and the generation of light-induced reactive oxygen species (ROS).[4,17–21] Another critical issue is the mismatch between the electron generation efficiency of semiconductor nanomaterials (*e.g.*, 3×10^{-11} s for CdS) and the electron utilization efficiency of methanogen metabolism (*e.g.*, 10^{-4} to 10^{-1} s for cytochrome-mediated processes), which leads to byproduct accumulation and reduced selectivity.[22] The high cost and biotoxicity associated with metal-based semiconductors also necessitate the development of new systems based on non-toxic, earth-abundant materials.

[a]*Key Laboratory of Low-grade Energy Utilization Technologies and Systems, Chongqing University, Chongqing 400044, China. E-mail: aoxia@cqu.edu.cn*

[b]*School of Energy and Power Engineering, Chongqing University, Chongqing 400044, China*

[c]*School of Chemical Engineering, Sichuan University, Chengdu 610065, China*

To address these limitations of suspended systems, we turned to nature for inspiration. In their natural habitats, microorganisms have evolved sophisticated strategies to cope with environmental stress and optimize resource exchange. Microorganisms predominantly exist in nature as structured communities known as biofilms, rather than as free-floating planktonic cells. Biofilms are three-dimensional structures embedded within a self-produced extracellular matrix.[23] This architecture provides internal cells with enhanced protection against environmental stresses and facilitates improved nutrient acquisition through metabolic cooperation.[24,25] Inspired by this natural organization, we propose a biofilm-based, semi-artificial photosynthetic system.

In the hybrid biofilm system, we employed a metal-free carbon nitride material as the photoelectric semiconductor. This material was modified by incorporating K^+ ions and grafting terminal cyano groups (–C≡N). This modification induced a positive zeta potential for cell attraction.[26,27] Moreover, this introduction of potassium ions serves as a Lewis acidic site, attracting extracellular polymeric substance (EPS) attachment through acid–base interactions.[28] $^{NCN}CN_x$, EPSs, and microbial cells self-assembled into a highly cross-linked network. Although not naturally formed, the self-assembled biofilm retains essential cells and key EPS components, consistent with the characterization of biofilms as microbial aggregates that typically accumulate at solid–liquid interfaces within a highly hydrated EPS matrix.[24] Furthermore, this system holds the potential to evolve into an organized multicellular structure with a complex three-dimensional architecture during subsequent growth. This structure enhanced material-cell interfacial binding, promoting the formation of a structurally robust biofilm.

The thin, dense biofilm allows for efficient light transmission and electron transfer, enabling superior performance under continuous illumination. Notably, the EPSs within the biofilm were also found to serve as scavengers of light-induced reactive oxygen species (ROS), thereby protecting the cells and retaining hybrid biofilm stability. The intrinsic properties of this biofilm significantly expand the hybrid system's capacity to utilize high-energy ultraviolet (UV) light, which accounts for approximately 5% of the solar spectrum. To address the mismatch between the electron uptake capacity of methanogens and the photoelectron generation rate of the semiconductor, we modified the cell surface with silver nanoparticles (Ag-NPs), achieving an exceptionally high quantum yield and methane production performance under continuous illumination. To the best of our knowledge, this study is the first to propose that it is the emergent properties of biofilms, arising from their collective multi-cellular assembly, that constitute an optimal framework for hybrid systems. This work offers inspiration for diverse semi-artificial photosynthesis configurations and opens up new avenues for designing practical hybrid biofilm reactors.

Results and discussion

Assembly of the hybrid biofilm

The carbon nitride before and after modification was characterized using Fourier-transform infrared spectroscopy (FT-IR) and X-ray photoelectron spectroscopy (XPS). In the FT-IR spectra (Fig. 1B), both materials exhibit an absorption peak at 810 cm^{-1}, corresponding to the breathing mode of triazine units. An absorption band in the range of 1150–1700 cm^{-1} is attributed to the stretching vibrations of C–N heterocycles. Compared with CN_x, $^{NCN}CN_x$ shows a new absorption band at 2180 cm^{-1}, which corresponds to the stretching vibration of the cyano group. Meanwhile, the N–H stretching vibration peak of $^{NCN}CN_x$ in the range of 2900–3600 cm^{-1} is significantly reduced, indicating successful bonding between the cyano groups and terminal amine groups of CN_x following modification.

Regarding elemental composition, $^{NCN}CN_x$ contains additional potassium (K) and trace amounts of sulfur (S) compared to CN_x (Fig. S1and S2). In the C 1s spectrum of $^{NCN}CN_x$ (Fig. 1C), three peaks are observed at 284.8, 285.9, and 288.1 eV, which are assigned to adventitious hydrocarbons, the cyano group, and the N–C=N bonds in the heptazine unit, respectively (Fig. 1C). In the N 1s spectrum (Fig. S3), three peaks appear at 398.5, 400.7, and 403.6 eV, corresponding to C–N=C, N–H bonds, and π-excitation, respectively. For the K 2p spectrum (Fig. 1C), the fitted peak can be indexed to metallic K (at 292.9 and 295.7 eV), which may be derived from K^+ adsorption within the heptazine rings.[29] The incorporation of K^+ leads to a more compact interlayer stacking, as evidenced by XRD analysis. Specifically, the diffraction angle of the (002) plane increases from the standard value of 27.4° (JCPDS 87-1526) to 28.4° (Fig. S4).[30] The synergistic effect of terminal cyano groups and incorporated K^+ ions induces a notable positive shift in the zeta potential of the intrinsically negative CN_x. This is attributed to the cyano groups withdrawing electron density from the framework, a process further amplified by the introduction of the positively charged potassium ions[31,32] (Fig. 1D).

Isothermal Titration Calorimetry (ITC) analysis revealed that the interaction between $^{NCN}CN_x$ and *M. barkeri* was a spontaneous binding process, yielding a Gibbs free energy change of binding (ΔG) of −27.20 kJ mol^{-1} and a binding constant (K_a) of 5.834×10^4. This binding was attributed to electrostatic interactions between $^{NCN}CN_x$ and the cell surface. Notably, the acid-treated $^{NCN}CN_x$ underwent the leaching of K^+ ions and the destruction of its cyano groups (Fig. S5),[27] and as a result, the acid-treated $^{NCN}CN_x$ lost its binding affinity for the cells, precluding the reliable determination of ΔG and K_a values (Fig. 1E). Furthermore, a significant spontaneous binding process was also observed between $^{NCN}CN_x$ and the isolated extracellular polymeric substances, with $\Delta G = -27.35$ kJ mol^{-1} and $K_a = 6.423 \times 10^4$ (Fig. S6). Scanning Electron Microscopy (SEM) images revealed that the $^{NCN}CN_x$ nanoparticles adsorbed onto and almost completely covered the entire cell surface (Fig. 1F). Transmission electron microscopy (TEM) images further confirm the attachment of $^{NCN}CN_x$ to *M. barkeri* cells, revealing small particles distributed around the cell surface (Fig. 1G). Under 365 nm light irradiation, aggregates composed of $^{NCN}CN_x$ and *M. barkeri* cells emit blue fluorescence, originating from the intrinsic bright blue fluorescence of $^{NCN}CN_x$ and the intracellular F420 enzyme (Fig. S7). FTIR analysis also confirms the coverage of cells by $^{NCN}CN_x$ (Fig. S8). Due to the cross-linked network among *M. barkeri* cells, EPSs, and $^{NCN}CN_x$

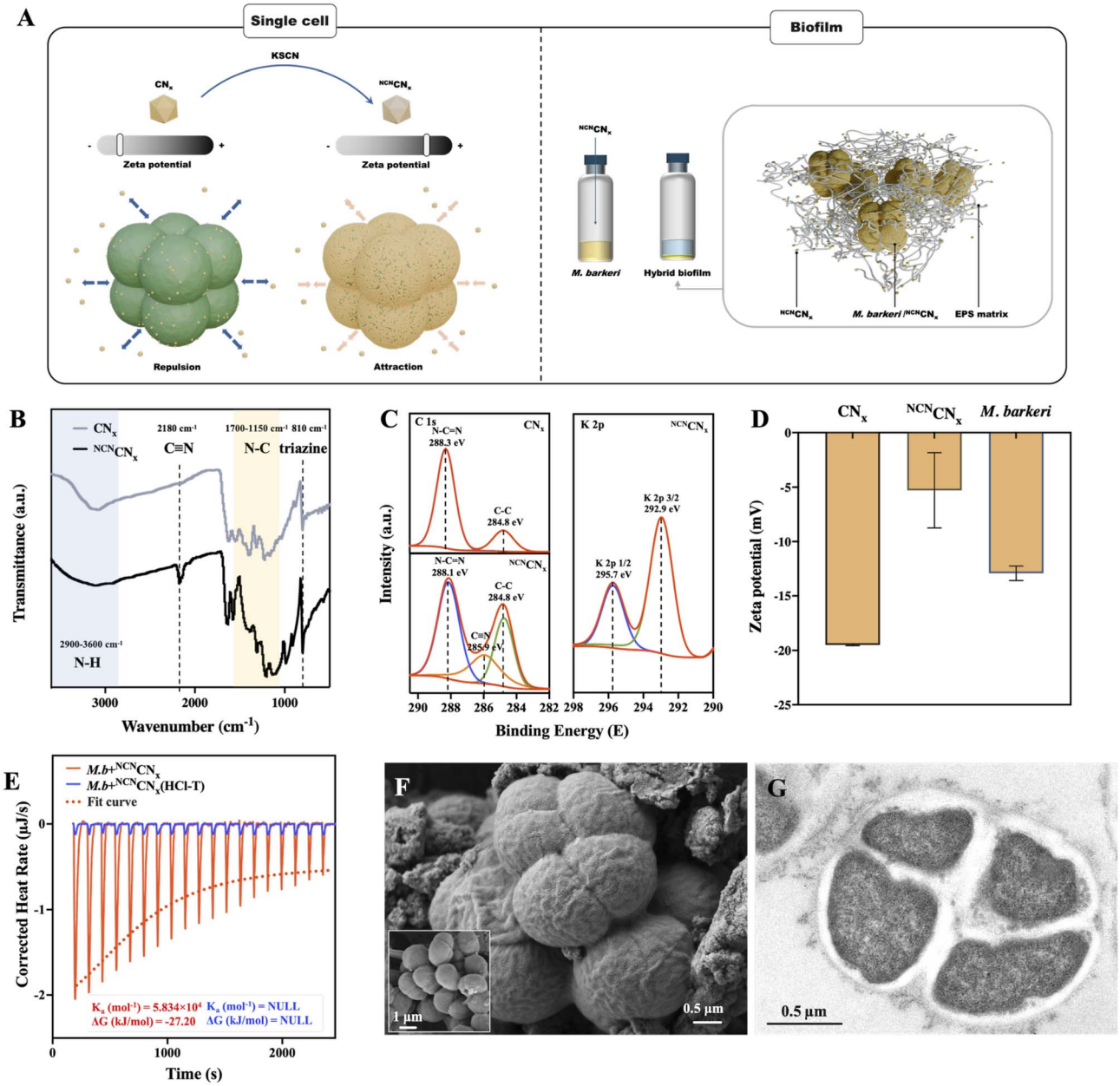

Fig. 1 Formation of hybrid biofilms. (A) Schematic illustration of hybrid single cells and hybrid biofilms. (B) FTIR spectra of CN_x and $^{NCN}CN_x$. (C) C 1s and K 2p XPS spectra of CN_x and $^{NCN}CN_x$. (D) Zeta potential of CN_x, $^{NCN}CN_x$, and *M. barkeri*. (E) Real-time ITC thermograms for the interactions of *M. barkeri* with $^{NCN}CN_x$ and with acid-treated $^{NCN}CN_x$. (F) SEM image of the $^{NCN}CN_x$/*M. barkeri* surface (the inset image shows bare *M. barkeri*). (G) TEM image of $^{NCN}CN_x$/*M. barkeri*.

(Fig. S9), the bio-hybrid was macroscopically observed as aggregated biofilm deposits at the bottom of the bottle (Fig. 1A) (Video S1).

Methane generation under illumination

The photocatalytic CO_2 reduction system for CH_4 production using hybrid biofilms was constructed and operated in a light incubator at a controlled temperature (35 °C) and a specific wavelength (395 ± 5 nm) (Fig. S10), to investigate the effects of light intensity on methane production. The results reveal that the methane production rate is positively correlated with light intensity (Fig. 2A and B), whereas the quantum yield shows a negative correlation, reaching its maximum value (1.5%) at the lowest light intensity tested (0.1 mW cm^{-2}) (Fig. 2E). Under illumination, a portion of the photogenerated electrons from $^{NCN}CN_x$ enter the intracellular metabolic pathway *via* membrane-integrated cytochromes of *M. barkeri* cells, while the other electrons reduce water at the $^{NCN}CN_x$ surface, producing hydrogen as a byproduct.[3,11] Under high-light intensity conditions, limited by the electron uptake capacity of *M. barkeri* cells and potential metabolic inhibition induced by photodamage, the proportion of electrons diverted to hydrogen production

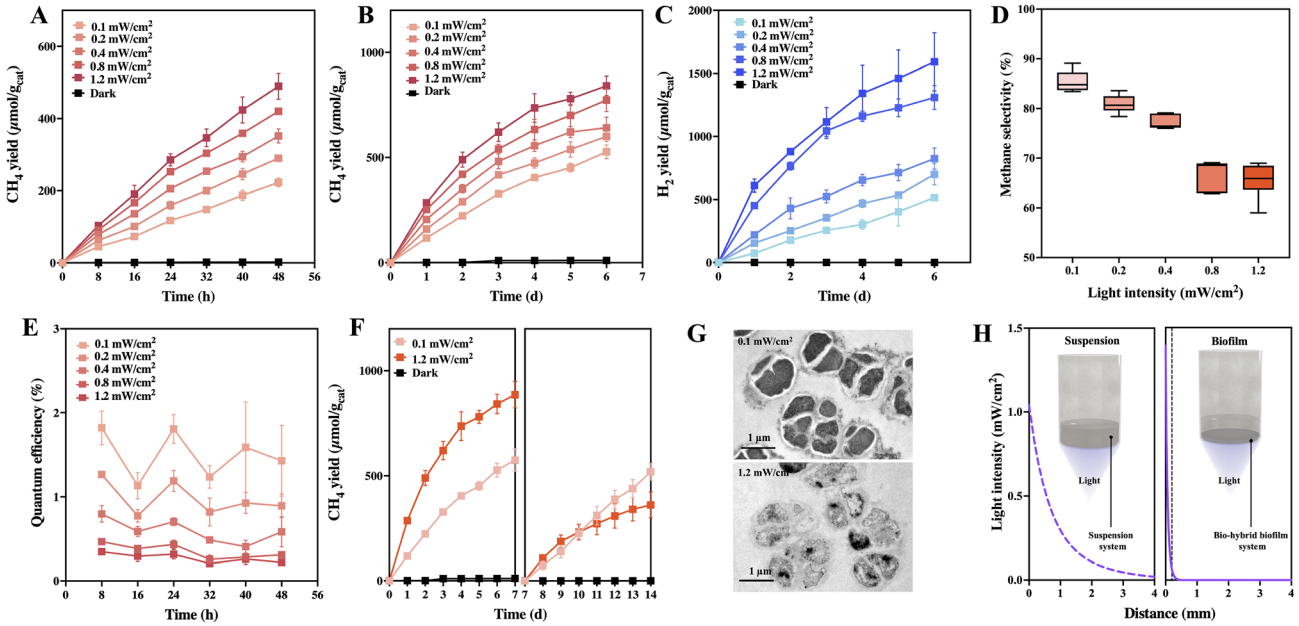

Fig. 2 Performance and characterization of hybrid biofilms. (A) Methane production within 48 hours. (B) Methane production within 6 days. (C) Hydrogen production within 6 days. (D) Methane selectivity over six days under continuous illumination (with one data point measured per day). (E) Methane quantum yield within 48 hours. (F) Comparison of methane production at high and low light intensity over 14 days. (G) TEM image of *M. barkeri* cells on day 14. (H) Light intensity distribution along the direction of illumination in suspension and biofilm systems.

increases from 14.55% (0.1 mW cm^{-2}) to 34.46% (1.0 mW cm^{-2}) (Fig. 2C and D). Although hybrid biofilms produce more methane at high light intensity, this condition adversely affects stability and selectivity, making it unsuitable for reliable long-term operation.

During the 48-hour illumination experiment, the quantum yield remained stable and CH_4 concentration increased linearly (Fig. S11). However, under six days of continuous illumination, the CH_4 production rate in the high-light-intensity group (1.0 mW cm^{-2}) exhibited a gradual decline (Fig. 2B and F), which can be attributed to a dual mechanism: mass transfer limitations arising from sacrificial reagent depletion in the bulk region and photodamage to cells induced by UV radiation. Notably, the decay in quantum yield observed in the low-light-intensity group (0.1 mW cm^{-2}) is primarily due to sacrificial reagent depletion rather than photodamage, which was validated by a 14-day long-term stability experiment on methane production (Fig. 2G). After replenishing the sacrificial reagent on day 7, the methane production performance of the high-light-intensity group in the second cycle dropped to only 40% of that in the first cycle. In contrast, the low-light-intensity group retained over 90% of its initial performance in the second cycle after the mass transfer limitations caused by sacrificial reagent depletion were alleviated. TEM imaging revealed marked differences in cellular morphology at different light intensities (Fig. 2H): cells exposed to low light intensity retained intact and well-defined structures, whereas those at high light intensity exhibited significant structural damage. The structure of the heteropolysaccharides on the outermost layer of the cell wall became indistinct, likely due to protein cross-linking or denaturation induced by UV exposure and reactive oxygen species (ROS)-mediated damage.[33–35] Loss of intracellular contents further led to the disappearance of the characteristic sarcina-like morphology. Unlike the optimal light intensity of 0.8–1.0 mW cm^{-2} reported in previous studies,[3,9,13] the hybrid biofilm in this study achieved excellent methane production performance at a much lower light intensity (0.1 mW cm^{-2}), attributed to more efficient light transmission.

Conventional hybrid systems typically employ suspended configurations, wherein microbial cells and solid photocatalyst particles may lack stable associations and remain dispersed throughout the liquid phase. This arrangement inherently hinders light penetration and distribution, often necessitating high incident light intensities to achieve adequate performance. However, such high intensities may lead to a non-uniform light field within the reactor, resulting in photodamage to cells near the light source while leaving cells deeper within the suspension light-limited.[36–38] In contrast, the *M. barkeri*/$^{NCN}CN_x$ combination developed in this study formed a dense, thin biofilm immobilized at the bottom of the vessel. This biofilm architecture presents distinct advantages for light delivery compared to suspended systems, achieving a 111.9% increase in methanogenesis performance under equivalent illumination conditions (11.9 μmol g_{cat}^{-1} h^{-1} *vs.* 5.6 μmol g_{cat}^{-1} h^{-1}) (Fig. S12). The biofilm configuration minimizes light scattering and absorption losses within the bulk liquid. Modeling simulations indicated that within the 4 mm-deep suspension, light intensity was attenuated by 90% at the vertical midpoint (a depth of 2 mm). However, the biofilm was concentrated at the bottom, a location that placed it within a region of relatively high irradiance and thereby enhanced its overall light utilization efficiency (Fig. 2H). While dense

biofilms may inherently impose mass transport resistance, potentially causing apoptosis of inner cells due to substrate depletion, this process is integral to the biofilm's lifecycle. The dynamic balance between gradient-driven apoptosis and the recruitment of new cells is crucial for sustaining the biofilm's long-term stability. Moreover, for small molecules like CO_2, the diffusion barrier is limited. The observed linear methane production rate under continuous illumination can serve as direct evidence.

Protection of EPSs against photodamage

Under continuous irradiation, the hybrid biofilm exhibited pronounced color changes: the initial white biofilm progressively turned blue with increasing light intensity (Fig. 3A). This color change originates from the intrinsic photophysical response of $^{NCN}CN_x$, rather than from the formation of organic radicals.[3] The cyano group and potassium ions within $^{NCN}CN_x$ modify its electronic structure, altering the HOMO–LUMO distribution, narrowing the bandgap, and suppressing the radiative decay of photoelectrons. Consequently, this promotes the accumulation of long-lived photoelectrons within the $^{NCN}CN_x$ conduction band, leading to the emergence of surface plasmon resonance (SPR).[39,40] This SPR results in broad optical absorption across the 500–800 nm spectral range, imparting the material's characteristic blue color observable macroscopically (Fig. S13). Notably, the color transition is reversible—upon termination of irradiation, the material gradually returns to its original white state through an electron release process, with the fading synchronized with the dissipation of accumulated electrons (Fig. S14) (Video S2). The experimental results indicate that deeper blue shades correspond to higher stored electron densities, which are still capable of driving biomethane production under dark conditions. However, the efficiency of methane synthesis in the dark is limited: photoelectron accumulation over 12 hours results in only a 20% increase in methane production during the subsequent 12-hour dark period (Fig. 3B). Although this additional dark-phase methane production can mathematically enhance the calculated quantum yield, it remains an inefficient strategy for methane synthesis under natural day/night cycles. In contrast, retaining stable and highly efficient photo–biocatalytic activity at constant low light intensity represents a more viable and effective approach.

During the experiment, a significant color change was also observed in the bulk solution: as the illumination time and light intensity increased, the solution gradually turned transparent orange-yellow (Fig. 3A). This phenomenon may be attributed to the release of the intracellular F420 cofactor. Three-dimensional fluorescence excitation-emission matrix (3D-EEM) analysis of the liquid phase after six days of exposure at varying light intensities revealed an increase in the characteristic peak intensity with increasing light intensity (Fig. 3C). Notably, the signal region ($E_x \approx 420$ nm and $E_m \approx 480$ nm) closely matched the spectral signature of the oxidized form of F420, a 5-deazaflavin F420.[41] UV-vis absorption spectroscopy further showed that the supernatant exhibited strong

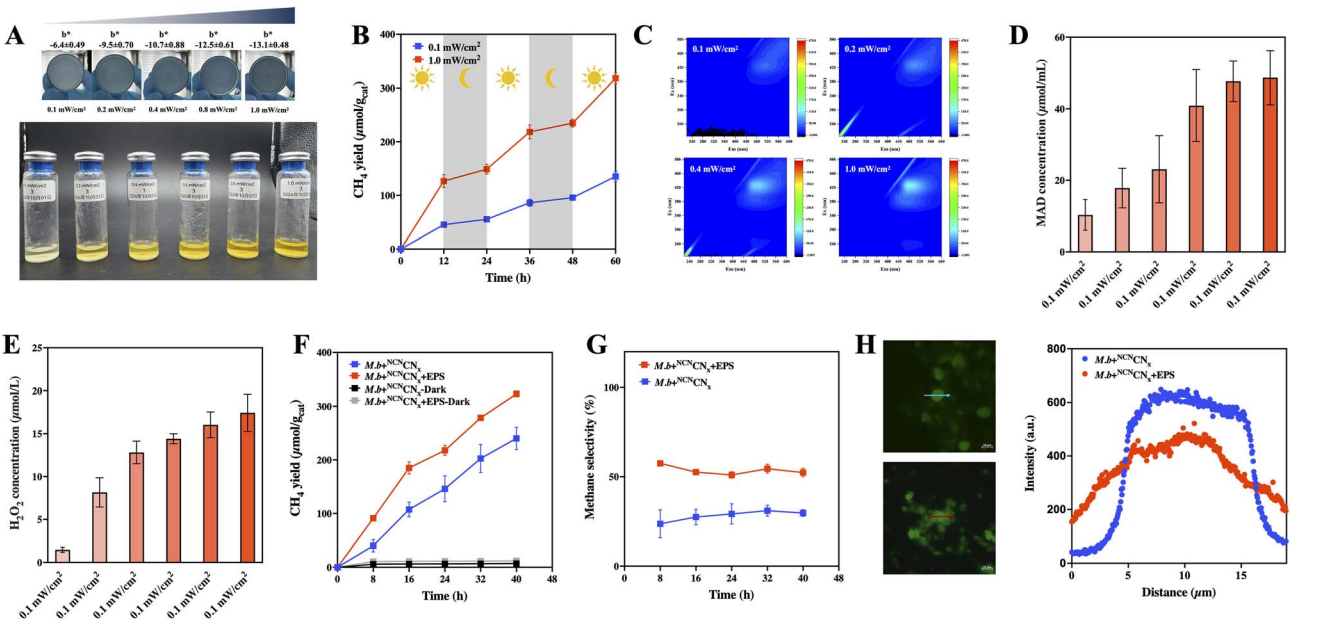

Fig. 3 Optical properties of hybrid biofilm systems under illumination, photodamage of biofilms, and the protective role of EPSs in hybrid biofilms. (A) Top: the biofilm at the bottom of the bottle turns blue under light (the inset numbers represent the mean CIE b^* values derived from digital colorimetric analysis, quantifying the intensification of the blue color). Bottom: the supernatant of the hybrid system turns yellow under light. (B) Methane production under light/dark cycles. (C) 3D-EEM analysis of the supernatant at varying light intensities. (D) MDA concentration at different light intensities. (E) H_2O_2 concentration at different light intensities. (F) Methane production under EPS addition. (G) Methane selectivity under EPS addition. (H) Left: fluorescence microscopy image of DCFDA-labeled cells. Right: fluorescence intensity at the marked positions on the fluorescent image.

absorption in the ultraviolet range (300–320 nm) across all tested intensities, likely corresponding to the reduced form of F420, which does not exhibit notable fluorescence (Fig. S15).[42,43] The prominent F420 signal in the high-light intensity group may indicate extensive cell lysis. Malondialdehyde (MDA), a key byproduct of lipid peroxidation and a well-established biomarker of oxidative cellular damage,[16] was found to increase with increasing light intensity (from 10.2 to 48.6 μmol mL^{-1}) (Fig. 3D). Additionally, the concentration of hydrogen peroxide (H_2O_2), a representative reactive oxygen species (ROS),[44] also showed a positive correlation with light intensity (ranging from 1.5 to 17.4 μmol mL^{-1}) (Fig. 3E). These findings collectively indicate that high-intensity UV-induced ROS are the primary drivers of cellular damage, causing membrane disruption and cell lysis and ultimately leading to the failure of the hybrid biofilm system.

The interaction between ROS and EPSs in biofilms was also investigated. When EPSs extracted from *M. barkeri* were co-incubated with H_2O_2 for 6 hours, the concentrations of extracellular proteins and polysaccharides decreased by 27.5% and 60.9%, respectively (Fig. S16). These findings indicate that the EPS matrix of hybrid biofilms may act as a sacrificial shield, degrading upon assault by ROS to preserve cellular viability.[45] Furthermore, 3D-EEM analysis was conducted to monitor the compositional evolution of EPS extracts both in isolation and in the presence of $^{NCN}CN_x$ under light irradiation (Fig. S17). The standalone EPS control exhibited no discernible changes in its fluorescence profile, suggesting that the incident light energy was insufficient to trigger direct photolysis. Conversely, the EPS-$^{NCN}CN_x$ mixture displayed a significant reduction in fluorescence intensity within the regions associated with fulvic acid-like and humic acid-like substances on days 3 and 6.[46] These findings underscore the critical role of photocatalytically generated ROS in mediating the oxidative degradation of EPS components. To evaluate the protective effects of EPSs under high light stress, hybrid biofilms supplemented with exogenous EPSs were subjected to high-intensity irradiation. Compared to control biofilms (lacking EPS supplementation), the EPS-supplemented systems exhibited a 34.6% increase in methane production (Fig. 3F) and a simultaneous 48.2% decrease in hydrogen byproduct production. Consequently, methane selectivity improved to 53.6%, substantially higher than the 28.2% recorded for the control group (Fig. 3G). Furthermore, assays using the DCFDA fluorescence probe indicated that intracellular ROS levels were 27.4% lower in cells within EPS-supplemented biofilms relative to the control (Fig. 3H).[47] These findings support the idea that EPSs provide cellular protection under light, likely by acting as a physical barrier and/or effectively scavenging ROS. The electrically conductive bio-interface formed by EPSs may also have contributed.[48] Although metal cocatalysts and heterojunctions can alleviate photocorrosion, applying these to semi-artificial systems is hindered by strict biocompatibility requirements and the difficulty of balancing interfacial charge transfer with ROS tolerance.[16] Intrinsic EPS components provide a more advantageous solution, effectively enabling the hybrid biofilm to harness the full solar spectrum.

Silver nanoparticles facilitate transmembrane electron transfer

Low quantum yields and byproduct accumulation in semi-artificial photosynthetic systems are often attributed to a kinetic mismatch between the rate of photogenerated electron supply from the semiconductor and the electron uptake capacity of the microbial cells. To mitigate this limitation, we investigated CO_2-to-CH_4 conversion performance in hybrid biofilms featuring *M. barkeri* cells surface-modified with silver nanoparticles (Ag-NPs). Cell viability was shown to be unaffected by the deposition of Ag-NPs, as confirmed by control experiments (Fig. S18). Energy-dispersive X-ray spectroscopy (EDS) imaging verified the successful anchoring of Ag-NPs onto the cell surface (Fig. 4A). In the hybrid system, the Ag-NPs shielded by carbon nitride exhibited a weaker EDS signal. Positioned between the cells and the $^{NCN}CN_x$, these Ag-NPs could serve as pathways for electron transfer, thereby facilitating the electron transfer process (Fig. 4B). Under illumination at 0.1 mW cm^{-2}, the Ag-NP-modified biofilm exhibited a 30% higher methane production rate and a 31% greater apparent quantum yield compared to unmodified controls (Fig. 4C and D). Concurrently, H_2 byproduct formation was substantially suppressed, leading to an 8% increase in methane selectivity (Fig. 4E). Cyclic voltammetry (CV) analysis revealed an enhanced cathodic current response from the Ag-NP-modified system near the potential associated with CO_2 reduction (−0.3 V *vs.* SCE) (Fig. S19). These electrochemical data, combined with conductivity measurements (Fig. S20), indicate that Ag-NPs facilitate extracellular electron transfer within the biofilm. A comparative analysis with existing methanogen-based hybrids suggests that achieving a high quantum yield and production yield at low light intensities is a prerequisite for the long-term, stable, and efficient operation of an ideal system (Fig. 4F). Most reported *Methanosarcina*-based hybrid systems rely on UV irradiation with intensities ranging from 0.8 to 5 mW cm^{-2}, typically achieving apparent quantum yields between 0.34% and 1.26% (with one study utilizing AM 1.5G simulated sunlight). In contrast, this work employs a hybrid biofilm architecture to significantly enhance photon utilization efficiency and improve robustness against ROS. The performance of hybrid systems under illumination is typically monitored over a period of 5–20 days; however, the ultimate stability at varying light intensities remains an unexplored gap in the field (Table S4). The system exhibited a stable methane production rate of 141.9 μmol g_{cat}^{-1} d^{-1}. Notably, this performance was achieved under continuous illumination at an unprecedentedly low intensity of 0.1 mW cm^{-2}, resulting in a quantum yield of 1.92%. A significant gap in current research is the lack of data on the long-term stability of hybrid systems under continuous illumination. Addressing this knowledge gap is paramount for assessing their viability for practical implementation.

The proteomes of *M. barkeri* in the hybrid biofilms of *M. barkeri*-$^{NCN}CN_x$ and Ag@*M. barkeri*-$^{NCN}CN_x$ were further analyzed using untargeted proteomics. A total of 2901 proteins were identified. Principal component analysis (PCA) revealed two distinct clusters, indicating that Ag-NP modification altered

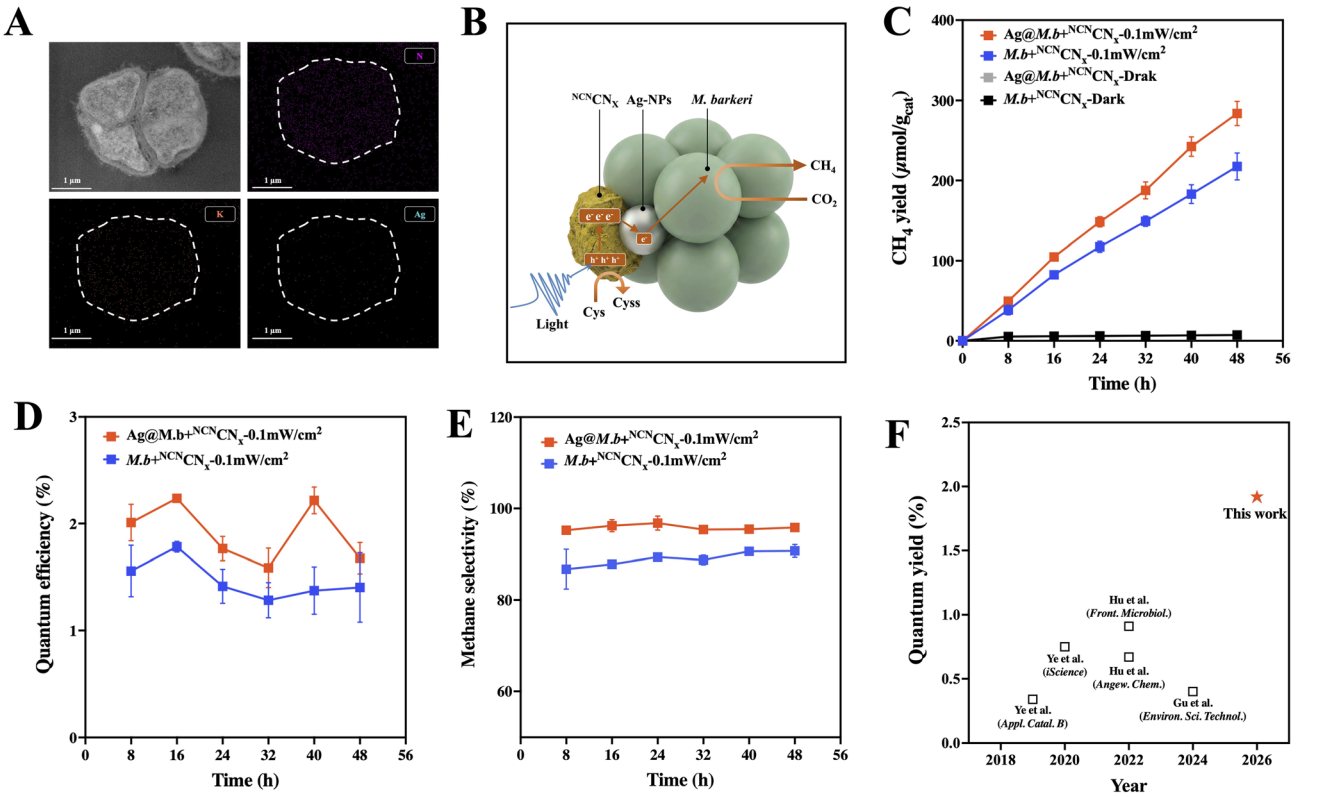

Fig. 4 Bioconversion characteristics of hybrid biofilms modified with Ag-NPs. (A) EDS mapping of *M. barkeri* cells modified with Ag-NPs. (B) Schematic illustration of electron transfer enhancement by Ag-NPs in the *M. barkeri*-$^{NCN}CN_x$ hybrid system. (C) Methane production using hybrid biofilms modified with Ag-NPs. (D) Quantum yield of hybrid biofilms modified with Ag-NPs. (E) Methane selectivity of hybrid biofilms modified with Ag-NPs. (F) Quantum yields reported in other relevant literature in recent years (under continuous illumination).

the physiological state of *M. barkeri* in the hybrid biofilms under light irradiation (Fig. 5A). In the Ag@*M. barkeri*-$^{NCN}CN_x$ system, 50 proteins were significantly upregulated (fold change >1.20 or $p < 0.05$) and 63 proteins were significantly downregulated (fold change <0.80 or $p < 0.05$) (Fig. 5B). Further functional analysis of differentially expressed proteins was performed using the Kyoto Encyclopedia of Genes and Genomes (KEGG) database. In addition to categories related to energy production and conversion (*C*), amino acid transport and metabolism (*E*), and secondary metabolite biosynthesis, transport, and catabolism (*Q*), multiple proteins involved in other diverse biological functions were also found to be upregulated.

To gain deeper insight into the underlying mechanisms, proteins involved in electron transfer, CO_2 conversion, and energy metabolism in *M. barkeri* were analyzed (Fig. 5D). Specifically, the enzymatic steps involved in the conversion of CO_2 to CH_4 are catalyzed by distinct protein complexes. Untargeted proteomics data revealed that formylmethanofuran dehydrogenase (Fmd) and methenyltetrahydromethanopterin cyclohydrolase (Mch) were significantly upregulated in Ag@*M. barkeri*-$^{NCN}CN_x$ hybrid biofilms compared to the control. These protein complexes catalyze the fixation of CO_2 onto methanofuran (MFR) and mediate the interconversion of formyl and methenyl oxidation states during C1 metabolism, playing essential roles in the early stages of methane formation.[49] The membrane-associated methyltransferase (Mtr), which catalyzes the transfer of the methyl group from methyl-tetrahydromethanopterin (CH_3-H_4MPT) to coenzyme M (CoM-SH),[50] was also significantly upregulated. Moreover, CobN-like chelatase BtuS—an essential corrinoid cofactor donor in the Mtr complex—showed increased expression.[51] Additionally, the biosynthesis pathway of coenzyme B, which is indispensable for the final methanogenesis step catalyzed by methyl-coenzyme M reductase (Mcr), was significantly enhanced. In this step, Mcr catalyzes the transfer of a methyl group from coenzyme M (CoM-SH) and reduces it to methane, utilizing coenzyme B (CoB-SH) as an electron donor.[52] In contrast, the down-regulation of MtaA (involved in methanol-dependent methanogenesis)[53] and MtmB (associated with dimethylamine-dependent methanogenesis)[54] suggests a metabolic shift in *M. barkeri*, where the CO_2 reduction pathway is prioritized over alternative substrate utilization pathways. Regarding energy metabolism, the upregulation of V-type ATP synthase subunits C and alpha, K^+-insensitive pyrophosphate-energized proton pump, and putative manganese-dependent inorganic pyrophosphatase indicates an increased demand for energy (in the form of ATP or proton gradient),[55] which is consistent with the observed enhancement in methane production.

Notably, under conditions that enhance methane production, ferredoxin—a key low-potential electron carrier—was significantly downregulated.[49] This reduction may indicate that

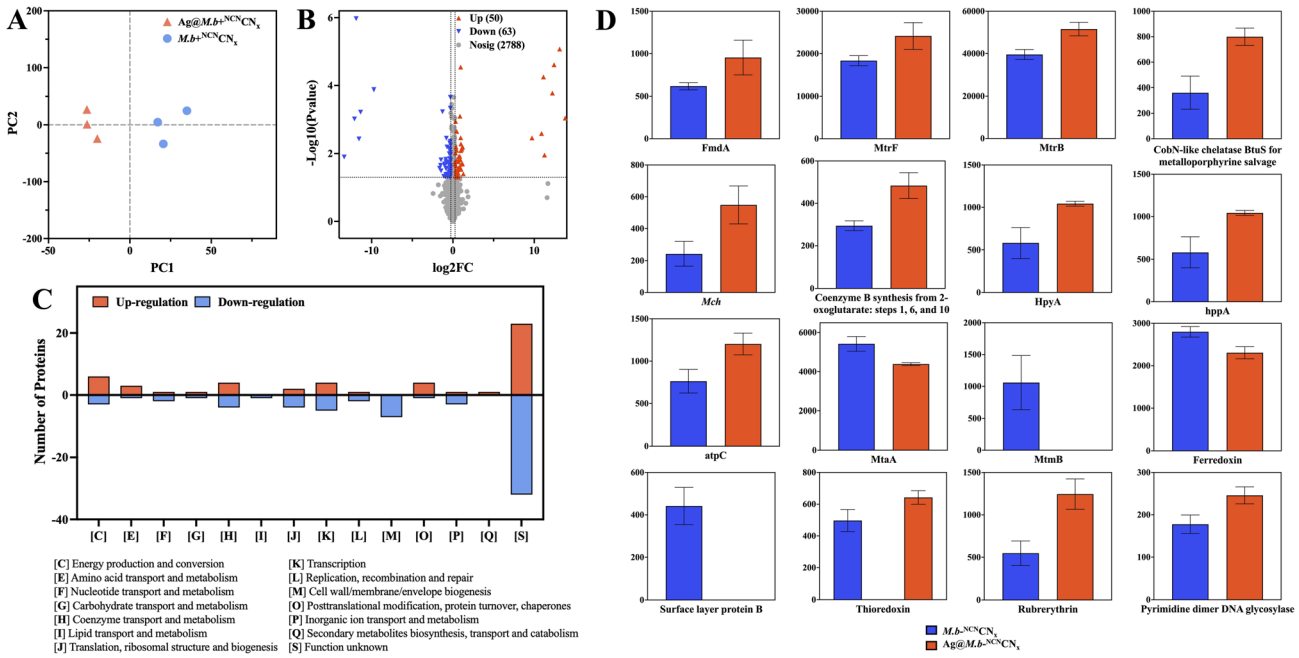

Fig. 5 Proteomic analysis of Ag@*M. barkeri*-$^{NCN}CN_x$ and *M. barkeri*-$^{NCN}CN_x$. (A) PCA plot of Ag@*M. barkeri*-$^{NCN}CN_x$ and *M. barkeri*-$^{NCN}CN_x$. (B) Volcano plot of Ag@*M. barkeri*-$^{NCN}CN_x$ and *M. barkeri*-$^{NCN}CN_x$. (C) KEGG functional annotation for proteins with significant variations in Ag@*M. barkeri*-$^{NCN}CN_x$ compared with *M. barkeri*-$^{NCN}CN_x$. (D) Relative concentration of proteins for electron transfer, energy conversion, CO_2 fixation, and oxidative stress response in Ag@*M. barkeri*-$^{NCN}CN_x$ compared with *M. barkeri*-$^{NCN}CN_x$.

the Ag-NPs attached to the cell surface provided an alternative electron transfer pathway, compensating for the decreased availability of ferredoxin (Fig. 6). The hydrogenase maturation factor HypA, which plays a critical role in the final assembly of [NiFe] active sites in the membrane-associated Vht and Frh hydrogenases,[56,57] was remarkably upregulated. This may suggest an increased flux of Fd-independent electrons from Vht to methyl-coenzyme M reductase (Mcr), partially compensating for the reduced ferredoxin levels.[49] Meanwhile, the Vht and Hdr complexes in *M. barkeri* contain membrane-bound cytochrome *b*, which is capable of directly accepting photoelectrons from the semiconductor.[58,59] The enhanced activity of these pathways indicates that the addition of Ag-NPs promotes cytochrome-mediated electron transfer, rather than relying on hydrogenase-mediated pathways such as those involving Ech. Additionally, a significant downregulation of surface layer protein B was observed in *M. barkeri* following Ag-NP modification, suggesting the integration of the nanoparticles into the cell membrane.[60,61] This incorporation may facilitate interactions with Vht and Hdr, leading to the formation of a novel electron transport pathway that enhances extracellular electron uptake. Moreover, the upregulation of rubrerythrin and thioredoxin (oxidative stress response)[62,63] and TldE (DNA repair-associated)[64] collectively indicates heightened oxidative stress in Ag@*M. barkeri*-$^{NCN}CN_x$ compared to the control.

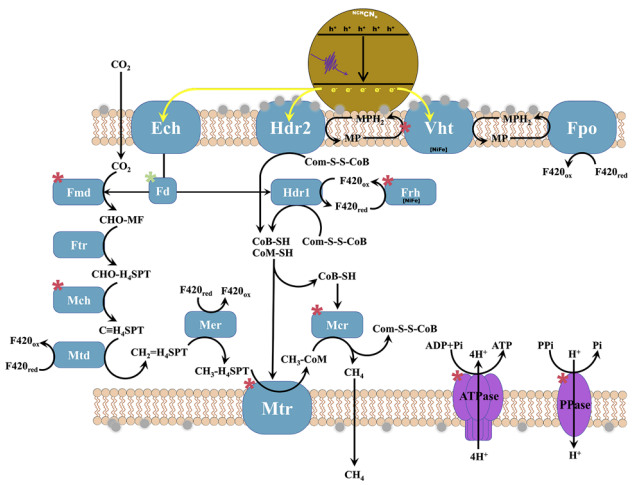

Fig. 6 Pathway of electron transfer and CO_2 reduction in Ag@*M. barkeri*-$^{NCN}CN_x$ (red*: upregulation and green*: downregulation).

Conclusions

In summary, a semi-artificial photosynthetic biofilm system was constructed, which achieved the efficient conversion of CO_2 to methane under continuous illumination. The tailored carbon nitride materials not only retain the excellent biocompatibility of metal-free photocatalysts, but the incorporation of K^+ ions and cyano groups also modulates their surface potential. This modification facilitates the efficient self-assembly of the materials with cells and extracellular polymeric substances, thereby constructing a mechanically robust biofilm featuring a cross-linked network. This architecture not only optimizes light absorption efficiency to enable high-performance conversion but also establishes an EPS-rich matrix as a natural barrier, attenuating the oxidative damage elicited by reactive oxygen

species. Furthermore, single-cell-level silver nanostructure modification further augments the intracellular ferredoxin-independent pathway, enabling the system to achieve unprecedented performance breakthroughs in the realm of semi-artificial photosynthesis: the final apparent quantum yield and product selectivity reached 1.92% and 97.1%, respectively.

While semi-artificial photosynthesis has achieved functional verification for various chemicals, low light utilization and photo-instability remain key engineering bottlenecks. Transitioning from suspended to biofilm systems surmounts these challenges, enabling versatile reactor designs through biofilm conformability. Rather than mere biomass accumulation, biofilms possess emergent properties driven by their internal heterogeneity. Future research targeting this heterogeneity will enable precise modulation of solute transport and electron transfer networks. Exploiting these features to engineer multi-species consortia promises a qualitative leap in catalytic efficiency for complex artificial photosynthetic systems.

Author contributions

H. C.: conceptualization, methodology, software, investigation, writing – original draft. A. X.: conceptualization, supervision, funding acquisition, writing – review & editing. Y. H.: software, validation, writing – review & editing. J. J.: methodology, writing – review & editing. J. Z.: methodology, visualization. X. Z.: software, visualization. X. Z.: resources, project administration. Q. L.: resources, supervision.

Conflicts of interest

There are no conflicts to declare.

Data availability

Additional data are available from the corresponding author upon reasonable request.

Supplementary information (SI): the experimental methods included in this study are described in detail in the SI. References 3, 9–12, 16, 65–71 are cited in the SI. See DOI: https://doi.org/10.1039/d6sc00459h.

Acknowledgements

This work was supported by the National Natural Science Foundation of China (No. 52376168 and 52021004), the Natural Science Foundation of Chongqing (No. CSTB2023NSCQ-JQX0005), and the Fundamental Research Funds for the Central Universities (No. 2024IAIS-ZD003).

Notes and references

1 Q. Wang and C. Pornrungroj, Artificial photosynthetic processes using carbon dioxide, water and sunlight: can they power a sustainable future?, *Chem. Sci.*, 2025, **16**, 18990–19011, DOI: 10.1039/d5sc03976b.

2 G. Zhou, Z. Wang, J. Gong, S. Shen and W. Zhong, Toward high-selectivity CO_2 photoelectroreduction: mechanistic foundations, recent advances and challenges, *Chem. Sci.*, 2025, **16**, 12718–12767, DOI: 10.1039/d5sc02284c.

3 A. Hu, J. Ye, G. Ren, Y. Qi, Y. Chen and S. Zhou, Metal-Free Semiconductor-Based Bio-Nano Hybrids for Sustainable CO_2-to-CH_4 Conversion with High Quantum Yield, *Angew. Chem., Int. Ed.*, 2022, **61**, e202206508, DOI: 10.1002/anie.202206508.

4 J. Ye, Y. Chen, C. Gao, C. Wang, A. Hu, G. Dong, Z. Chen, S. Zhou and Y. Xiong, Sustainable Conversion of Microplastics to Methane with Ultrahigh Selectivity by a Biotic–Abiotic Hybrid Photocatalytic System, *Angew. Chem., Int. Ed.*, 2022, **61**, e202213244, DOI: 10.1002/anie.202213244.

5 C. Zhong, Y. Ren, Y.-Y. Guo, A. Lu and J. Liu, Photoelectron-Promoted Sulfate Reduction for Heavy Metal Removal without Organic Carbon Addition, *Environ. Sci. Technol.*, 2024, **58**, 21680–21691, DOI: 10.1021/acs.est.4c08073.

6 W. Kang, L. Mu and X. Hu, Marine Colloids Boost Nitrogen Fixation in *Trichodesmium erythraeum* by Photoelectrophy, *Environ. Sci. Technol.*, 2024, **58**, 9236–9249, DOI: 10.1021/acs.est.4c01849.

7 J. Guo, M. Suástegui, K. K. Sakimoto, V. M. Moody, G. Xiao, D. G. Nocera and N. S. Joshi, Light-driven fine chemical production in yeast biohybrids, *Science*, 2018, **362**, 813–816, DOI: 10.1126/science.aat9777.

8 S. Wang, L. Mu, Q. Qu, X. Hu and F. Wu, Intracellular–Extracellular Synergistic Biohybrid System Boosts Photosynthetic Carbon Fixation, *Environ. Sci. Technol.*, 2025, **59**, 12717–12729, DOI: 10.1021/acs.est.5c05048.

9 S. Kalathil, M. Rahaman, E. Lam, T. L. Augustin, H. F. Greer and E. Reisner, Solar-Driven Methanogenesis through Microbial Ecosystem Engineering on Carbon Nitride, *Angew. Chem., Int. Ed.*, 2024, **63**, e202409192, DOI: 10.1002/anie.202409192.

10 A. Hu, T. Fu, G. Ren, M. Zhuang, W. Yuan, S. Zhong and S. Zhou, Sustained Biotic-Abiotic Hybrids Methanogenesis Enabled Using Metal-Free Black Phosphorus/Carbon Nitride, *Front. Microbiol.*, 2022, **13**, 2022, DOI: 10.3389/fmicb.2022.957066.

11 J. Ye, J. Yu, Y. Zhang, M. Chen, X. Liu, S. Zhou and Z. He, Light-driven carbon dioxide reduction to methane by *Methanosarcina barkeri*-CdS biohybrid, *Appl. Catal., B*, 2019, **257**, 117916, DOI: 10.1016/j.apcatb.2019.117916.

12 J. Ye, G. Ren, L. Kang, Y. Zhang, X. Liu, S. Zhou and Z. He, Efficient Photoelectron Capture by Ni Decoration in *Methanosarcina barkeri*-CdS Biohybrids for Enhanced Photocatalytic CO_2-to-CH_4 Conversion, *iScience*, 2020, **23**(7), 101287, DOI: 10.1016/j.isci.2020.101287.

13 J. Ye, C. Wang, C. Gao, T. Fu, C. Yang, G. Ren, J. Lü, S. Zhou and Y. Xiong, Solar-driven methanogenesis with ultrahigh selectivity by turning down H_2 production at biotic-abiotic interface, *Nat. Commun.*, 2022, **13**, 6612, DOI: 10.1038/s41467-022-34423-1.

14 T. Zhi, T. Fu, H. Zhan, R. Zhou, M. Yang, C. Gao, P. Wang, S. Zhan and Q. Zhou, Photosynthetic Biohybrid Systems: A

Promising Approach for Energy and Environmental Applications, *Environ. Sci. Technol.*, 2025, **59**, 16090–16111, DOI: 10.1021/acs.est.5c04721.

15 M. Rahaman, C. Pulignani, M. Miller, S. Bhattacharjee, A. Bin Mohamad Annuar, R. R. Manuel, I. A. C. Pereira and E. Reisner, Solar-Driven Paired CO_2 Reduction–Alcohol Oxidation Using Semiartificial Suspension, Photocatalyst Sheet, and Photoelectrochemical Devices, *J. Am. Chem. Soc.*, 2025, **147**, 8168–8177, DOI: 10.1021/jacs.4c10519.

16 W. Gu, J. Hu, L. Li, M. Hong, C. Yang, G. Ren, J. Ye and S. Zhou, Natural AIEgens as Ultraviolet Sunscreens and Photosynergists for Solar Fuel Production, *Environ. Sci. Technol.*, 2024, **58**, 20434–20443, DOI: 10.1021/acs.est.4c05605.

17 K. Pullerits, J. Ahlinder, L. Holmer, E. Salomonsson, C. Öhrman, K. Jacobsson, R. Dryselius, M. Forsman, C. J. Paul and P. Rådström, Impact of UV irradiation at full scale on bacterial communities in drinking water, *npj Clean Water*, 2020, **3**, 11, DOI: 10.1038/s41545-020-0057-7.

18 A. L. Santos, C. Moreirinha, D. Lopes, A. C. Esteves, I. Henriques, A. Almeida, M. R. M. Domingues, I. Delgadillo, A. Correia and Â. Cunha, Effects of UV Radiation on the Lipids and Proteins of Bacteria Studied by Mid-Infrared Spectroscopy, *Environ. Sci. Technol.*, 2013, **47**, 6306–6315, DOI: 10.1021/es400660g.

19 A. L. Santos, V. Oliveira, I. Baptista, I. Henriques, N. C. M. Gomes, A. Almeida, A. Correia and Â. Cunha, Wavelength dependence of biological damage induced by UV radiation on bacteria, *Arch. Microbiol.*, 2013, **195**, 63–74, DOI: 10.1007/s00203-012-0847-5.

20 C. Wang, J. Yu, G. Ren, A. Hu, X. Liu, Y. Chen, J. Ye, S. Zhou and Z. He, Self-replicating biophotoelectrochemistry system for sustainable CO methanation, *Environ. Sci. Technol.*, 2022, **56**, 4587–4596, DOI: 10.1021/acs.est.1c08340.

21 X. Chen, Q. Feng, Q. Cai, S. Huang, Y. Yu, R. J. Zeng, M. Chen and S. Zhou, Mn_3O_4 nanozyme coating accelerates nitrate reduction and decreases N_2O emission during photoelectrotrophic denitrification by *Thiobacillus denitrificans*-CdS, *Environ. Sci. Technol.*, 2020, **54**, 10820–10830, DOI: 10.1021/acs.est.0c02709.

22 I. L. Bishara Robertson, H. Zhang, E. Reisner, J. N. Butt and L. J. C. Jeuken, Engineering of bespoke photosensitiser–microbe interfaces for enhanced semi-artificial photosynthesis, *Chem. Sci.*, 2024, **15**, 9893–9914, DOI: 10.1039/d4sc00864b.

23 Ü. Akbey and M. Andreasen, Functional amyloids from bacterial biofilms – structural properties and interaction partners, *Chem. Sci.*, 2022, **13**, 6457–6477, DOI: 10.1039/d2sc00645f.

24 H.-C. Flemming and J. Wingender, The biofilm matrix, *Nat. Rev. Microbiol.*, 2010, **8**, 623–633, DOI: 10.1038/nrmicro2415.

25 Z. You, J. Li, Y. Wang, D. Wu, F. Li and H. Song, Advances in mechanisms and engineering of electroactive biofilms, *Biotechnol. Adv.*, 2023, **66**, 108170, DOI: 10.1016/j.biotechadv.2023.108170.

26 S. J. Goncher, L. Zhao, A. N. Pasupathy and G. W. Flynn, Substrate Level Control of the Local Doping in Graphene, *Nano Lett.*, 2013, **13**, 1386–1392, DOI: 10.1021/nl3039508.

27 E. Hu, Q. Chen, Q. Gao, X. Fan, X. Luo, Y. Wei, G. Wu, H. Deng, S. Xu, P. Wang, L. Liu, R. He, X. Chen, W. Zhu and Y. Zhu, Cyano-Functionalized Graphitic Carbon Nitride with Adsorption and Photoreduction Isosite Achieving Efficient Uranium Extraction from Seawater, *Adv. Funct. Mater.*, 2024, **34**, 2312215, DOI: 10.1002/adfm.202312215.

28 C.-c. Ji, H. Zhou, S.-K. Deng, K.-Y. Chen, X.-Y. Dong, X.-H. Xu and L.-H. Cheng, Insight into the adhesion propensities of extracellular polymeric substances (EPS) on the abiotic surface using XDLVO theory, *J. Environ. Chem. Eng.*, 2021, **9**, 106563, DOI: 10.1016/j.jece.2021.106563.

29 J. Wang, Y. Qin, L. Li, S. Zhang, X. Pei, Z. Niu, X.-C. Zheng and D. Li, Defective engineering and heteroatom doping construction in carbon nanobowls for achieving high-rate potassium-ion storage with long cyclic life, *Chem. Eng. J.*, 2023, **457**, 141253, DOI: 10.1016/j.cej.2022.141253.

30 V. W.-h. Lau, I. Moudrakovski, T. Botari, S. Weinberger, M. B. Mesch, V. Duppel, J. Senker, V. Blum and B. V. Lotsch, Rational design of carbon nitride photocatalysts by identification of cyanamide defects as catalytically relevant sites, *Nat. Commun.*, 2016, **7**, 12165, DOI: 10.1038/ncomms12165.

31 Y. Liu, C. Pulignani, S. Webb, S. J. Cobb, S. Rodríguez-Jiménez, D. Kim, R. D. Milton and E. Reisner, Electrostatic [FeFe]-hydrogenase–carbon nitride assemblies for efficient solar hydrogen production, *Chem. Sci.*, 2024, **15**, 6088–6094, DOI: 10.1039/d4sc00640b.

32 H. Chang, X. Liu, A. Xia, W. Zhu, J. Ji, X. Zhu, J. Zhang, Y. Huang, X. Zhu and Q. Liao, How can thermoelectric coupling catalysis be applied to facilitate biomass conversion into value-added products and hydrogen?, *Chem. Soc. Rev.*, 2026, DOI: 10.1039/d5cs00320b.

33 K. Xiao, T. Wang, M. Sun, A. Hanif, Q. Gu, B. Tian, Z. Jiang, B. Wang, H. Sun, J. Shang and P. K. Wong, Photocatalytic Bacterial Inactivation by a Rape Pollen-MoS_2 Biohybrid Catalyst: Synergetic Effects and Inactivation Mechanisms, *Environ. Sci. Technol.*, 2020, **54**, 537–549, DOI: 10.1021/acs.est.9b05627.

34 J. B. Robertson, C. R. Davis and C. H. Johnson, Visible light alters yeast metabolic rhythms by inhibiting respiration, *Proc. Natl. Acad. Sci. U. S. A.*, 2013, **110**, 21130–21135, DOI: 10.1073/pnas.1313369110.

35 K. Xiao, J. Liang, X. Wang, T. Hou, X. Ren, P. Yin, Z. Ma, C. Zeng, X. Gao, T. Yu, T. Si, B. Wang, C. Zhong, Z. Jiang, C.-S. Lee, J. C.-m. Yu and P. K. Wong, Panoramic insights into semi-artificial photosynthesis: origin, development, and future perspective, *Energy Environ. Sci.*, 2022, **15**, 529–549, DOI: 10.1039/d1ee03094a.

36 S. T. Chua, A. Smith, S. Murthy, M. Murace, H. Yang, L. Schertel, M. Kühl, P. Cicuta, A. G. Smith, D. Wangpraseurt and S. Vignolini, Light management by algal aggregates in living photosynthetic hydrogels, *Proc.*

Natl. Acad. Sci. U. S. A., 2024, **121**, e2316206121, DOI: 10.1073/pnas.2316206121.

37 S. Zhou, J. Duan, J. Shi, S. Fan, G. Chen and X. Li, Enhanced solar-driven semiconductor–Bacteria biohybrids system for N_2 reduction into ammonia, *Appl. Catal., B*, 2025, **377**, 125513, DOI: 10.1016/j.apcatb.2025.125513.

38 X. Fang, S. Kalathil and E. Reisner, Semi-biological approaches to solar-to-chemical conversion, *Chem. Soc. Rev.*, 2020, **49**, 4926–4952, DOI: 10.1039/c9cs00496c.

39 D. Tian, H. Yin, L. Liu, B. Li, J. Li and Z. Lou, Plasmonic Carbon Nitride Polymers to Boost Hydrogen Generation, *Adv. Sustainable Syst.*, 2022, **6**, 2200045, DOI: 10.1002/adsu.202200045.

40 J. Bian, X. An, J. Zhao, Y. Liao, X. Lan, R. Liu, C. Hu, J.-j. Chen, H. Liu and J. Qu, Directional Electron Transfer in Enzymatic Nano-Bio Hybrids for Selective Photobiocatalytic Conversion of Nitrate, *Angew. Chem., Int. Ed.*, 2024, **63**, e202412194, DOI: 10.1002/anie.202412194.

41 P. Popova, L. Astete Vasquez, S. Bolden and N. Mladenov, Enrichment of anammox bacteria in up-flow bioreactors enhanced with plastic and rock media: Long-term performance monitoring with fluorescence and specific conductivity, *Bioresour. Technol. Rep.*, 2025, **29**, 102081, DOI: 10.1016/j.biteb.2025.102081.

42 K. D. Ashby, T. A. Casey, M. A. Rasmussen and J. W. Petrich, Steady-State and Time-Resolved Spectroscopy of F420 Extracted from Methanogen Cells and Its Utility as a Marker for Fecal Contamination, *J. Agric. Food Chem.*, 2001, **49**, 1123–1127, DOI: 10.1021/jf000689r.

43 C. Greening, F. H. Ahmed, A. E. Mohamed, M. Lee Brendon, G. Pandey, C. Warden Andrew, C. Scott, G. Oakeshott John, C. Taylor Matthew and J. Jackson Colin, Physiology, Biochemistry, and Applications of F420- and Fo-Dependent Redox Reactions, *Microbiol. Mol. Biol. Rev.*, 2016, **80**, 451–493, DOI: 10.1128/mmbr.00070-15.

44 M. Zhao, J. Shi, Z. Zhao, D. Zhou and S. Dong, Enhancing chlorophenol biodegradation: Using a co-substrate strategy to resist photo-H_2O_2 stress in a photocatalytic-biological reactor, *Chem. Eng. J.*, 2018, **352**, 255–261, DOI: 10.1016/j.cej.2018.07.018.

45 M. A. Khalil, F. I. Sonbol, L. A. Al-Madboly, T. A. Aboshady, A. S. Alqurashi and S. S. Ali, Exploring the Therapeutic Potentials of Exopolysaccharides Derived From Lactic Acid Bacteria and Bifidobacteria: Antioxidant, Antitumor, and Periodontal Regeneration, *Front. Microbiol.*, 2022, **13**, 803688, DOI: 10.3389/fmicb.2022.803688.

46 A. Hu, B. Li, S. Yang, C. Yang, J. Ye, Y. Huang, S. Zhou and G. Wang, Unlocking interfacial electron transfer in biophotoelectrochemical processes: Role of extracellular polymeric substances in aquatic environments, *Water Res.*, 2025, **278**, 123375, DOI: 10.1016/j.watres.2025.123375.

47 Y. Li, C. Shen, X. Zhou, J. Zhang, X. Lai and Y. Zhang, Local Treatment of Hydrogen-Rich Saline Promotes Wound Healing *In Vivo* by Inhibiting Oxidative Stress *via* Nrf-2/HO-1 Pathway, *Oxid. Med. Cell. Longevity*, 2022, **2022**, 2949824, DOI: 10.1155/2022/2949824.

48 H. Li, J. Lu, G. Owens and Z. Chen, Extracellular polymeric substances bestowed effective interfacial electron transfer process during biohybrid-activated periodate: Dual enhancement of hydrophilicity and electron conductivity, *Appl. Catal., B*, 2026, **380**, 125797, DOI: 10.1016/j.apcatb.2025.125797.

49 D. Mand Thomas and W. Metcalf William, Energy Conservation and Hydrogenase Function in Methanogenic Archaea, in Particular the Genus *Methanosarcina*, *Microbiol. Mol. Biol. Rev.*, 2019, **83**(4), e00020, DOI: 10.1128/mmbr.00020-19.

50 C. Schöne, A. Poehlein and M. Rother, Genetic and Physiological Probing of Cytoplasmic Bypasses for the Energy-Converting Methyltransferase Mtr in *Methanosarcina acetivorans*, *Appl. Environ. Microbiol.*, 2023, **89**(7), e02161, DOI: 10.1128/aem.02161-22.

51 H. Fausset, L. Spietz Rachel, S. Cox, G. Cooper, S. Spurzem, M. Tokmina-Lukaszewska, J. DuBois, B. Broderick Joan, M. Shepard Eric, S. Boyd Eric and B. Bothner, A shift between mineral and nonmineral sources of iron and sulfur causes proteome-wide changes in *Methanosarcina barkeri*, *Microbiol. Spectrum*, 2024, **12**, e00418–e00423, DOI: 10.1128/spectrum.00418-23.

52 T.-A. Dinh and K. D. Allen, Toward the Use of Methyl-Coenzyme M Reductase for Methane Bioconversion Applications, *Acc. Chem. Res.*, 2024, **57**, 2746–2757, DOI: 10.1021/acs.accounts.4c00413.

53 Y. Cao, J. Li, N. Jiang and X. Dong, Mechanism for Stabilizing mRNAs Involved in Methanol-Dependent Methanogenesis of Cold-Adaptive *Methanosarcina mazei zm-15*, *Appl. Environ. Microbiol.*, 2014, **80**, 1291–1298, DOI: 10.1128/AEM.03495-13.

54 D. D. Nayak and W. W. Metcalf, Methylamine-specific methyltransferase paralogs in *Methanosarcina* are functionally distinct despite frequent gene conversion, *ISME J.*, 2019, **13**, 2173–2182, DOI: 10.1038/s41396-019-0428-6.

55 I. B. Schäfer, S. M. Bailer, M. G. Düser, M. Börsch, R. A. Bernal, D. Stock and G. Grüber, Crystal Structure of the Archaeal A1AO ATP Synthase Subunit B from *Methanosarcina mazei Gö1*: Implications of Nucleotide-binding Differences in the Major A1AO Subunits A and B, *J. Mol. Biol.*, 2006, **358**, 725–740, DOI: 10.1016/j.jmb.2006.02.057.

56 K.-H. Chan, K.-M. Lee and K.-B. Wong, Interaction between Hydrogenase Maturation Factors HypA and HypB Is Required for [NiFe]-Hydrogenase Maturation, *PLoS One*, 2012, **7**, e32592, DOI: 10.1371/journal.pone.0032592.

57 K. Miki, H. Atomi and S. Watanabe, Structural Insight into [NiFe] Hydrogenase Maturation by Transient Complexes between Hyp Proteins, *Acc. Chem. Res.*, 2020, **53**, 875–886, DOI: 10.1021/acs.accounts.0c00022.

58 N. Kornienko, K. K. Sakimoto, D. M. Herlihy, S. C. Nguyen, A. P. Alivisatos, C. B. Harris, A. Schwartzberg and P. Yang, Spectroscopic elucidation of energy transfer in hybrid inorganic–biological organisms for solar-to-chemical

production, *Proc. Natl. Acad. Sci. U. S. A.*, 2016, **113**, 11750–11755, DOI: 10.1073/pnas.1610554113.

59 J. Ye, A. Hu, G. Ren, M. Chen, J. Tang, P. Zhang, S. Zhou and Z. He, Enhancing sludge methanogenesis with improved redox activity of extracellular polymeric substances by hematite in red mud, *Water Res.*, 2018, **134**, 54–62, DOI: 10.1016/j.watres.2018.01.062.

60 L. Rohlin, D. R. Leon, U. Kim, J. A. Loo, R. R. Ogorzalek Loo and R. P. Gunsalus, Identification of the Major Expressed S-Layer and Cell Surface-Layer-Related Proteins in the Model Methanogenic Archaea: *Methanosarcina barkeri Fusaro* and *Methanosarcina acetivorans C2A*, *Archaea*, 2012, **2012**, 873589, DOI: 10.1155/2012/873589.

61 V. Milkevych, B. C. Donose, N. Juste-Poinapen and D. J. Batstone, Mechanical and cell-to-cell adhesive properties of aggregated *Methanosarcina*, *Colloids Surf., B*, 2015, **126**, 303–312, DOI: 10.1016/j.colsurfb.2014.12.035.

62 W. Zhang, D. E. Culley, M. Hogan, L. Vitiritti and F. J. Brockman, Oxidative stress and heat-shock responses in *Desulfovibrio vulgaris* bygenome-wide transcriptomic analysis, *Antonie van Leeuwenhoek*, 2006, **90**, 41–55, DOI: 10.1007/s10482-006-9059-9.

63 M. Balsera and B. B. Buchanan, Evolution of the thioredoxin system as a step enabling adaptation to oxidative stress, *Free Radical Biol. Med.*, 2019, **140**, 28–35, DOI: 10.1016/j.freeradbiomed.2019.03.003.

64 M. Kopf, F. Möke, H. Bauwe, W. R. Hess and M. Hagemann, Expression profiling of the bloom-forming *Cyanobacterium Nodularia CCY9414* under light and oxidative stress conditions, *ISME J.*, 2015, **9**, 2139–2152, DOI: 10.1038/ismej.2015.16.

65 M. Chen, Q. Cai, X. Chen, S. Huang, Q. Feng, T. Majima, R. J. Zeng and S. Zhou, Anthraquinone-2-Sulfonate as a Microbial Photosensitizer and Capacitor Drives Solar-to-N_2O Production with a Quantum Efficiency of Almost Unity, *Environ. Sci. Technol.*, 2022, **56**, 5161–5169, DOI: 10.1021/acs.est.1c08710.

66 C. Gu, P. Gao, F. Yang, D. An, M. Munir, H. Jia, G. Xue and C. Ma, Characterization of extracellular polymeric substances in biofilms under long-term exposure to ciprofloxacin antibiotic using fluorescence excitation-emission matrix and parallel factor analysis, *Environ. Sci. Pollut. Res.*, 2017, **24**, 13536–13545, DOI: 10.1007/s11356-017-8986-5.

67 H. Kasap, D. S. Achilleos, A. Huang and E. Reisner, Photoreforming of Lignocellulose into H_2 Using Nanoengineered Carbon Nitride under Benign Conditions, *J. Am. Chem. Soc.*, 2018, **140**, 11604–11607, DOI: 10.1021/jacs.8b07853.

68 S. D. Gardner, C. S. K. Singamsetty, G. L. Booth, G.-R. He and C. U. Pittman, Surface characterization of carbon fibers using angle-resolved XPS and ISS, *Carbon*, 1995, **33**, 587–595, DOI: 10.1016/0008-6223(94)00144-O.

69 F. Loosli, L. Vitorazi, J.-F. Berret and S. Stoll, Towards a better understanding on agglomeration mechanisms and thermodynamic properties of TiO_2 nanoparticles interacting with natural organic matter, *Water Res.*, 2015, **80**, 139–148, DOI: 10.1016/j.watres.2015.05.009.

70 J. Fang, D. Wang, H. Xu, F. Sun, Y. Fan, R. Chen and Q. Liu, Unleashing solar energy's full potential: Synergetic thermo-photo catalysis for enhanced hydrogen production with metal-free carbon nitrides, *Energy Convers. Manage.*, 2024, **300**, 117995, DOI: 10.1016/j.enconman.2023.117995.

71 R. Xia, J. Cheng, Z. Chen, Z. Zhang, X. Zhou, J. Zhou and M. Zhang, Revealing Co-N_4@Co-NP Bridge-Enabled Fast Charge Transfer and Active Intracellular Methanogenesis in Bio-Electrochemical CO_2-Conversion with *Methanosarcina Barkeri*, *Adv. Mater.*, 2023, **35**(52), 2304920, DOI: 10.1002/adma.202304920.